

# Pyrolysis of Schiff-Base Manganese Clusters: Effect of Ligand Modulation on the Performance of Supercapacitor Electrodes

Jianing Li<sup>+</sup><sup>[a]</sup>, Kai Zhao<sup>+</sup><sup>[a]</sup>, Tian Li,<sup>[a]</sup> Yuxin Shi,<sup>[a]</sup> Yuebin Li,<sup>\*[a]</sup> and Xu Peng<sup>\*[a]</sup>

Ligand modulation on metal organic clusters endow them with different physical and chemical properties, while how ligand modulation further affects the electrochemical behavior of pyrolytic derivatives is still unclear. Herein, we constructed two trinuclear manganese clusters **1-Mn<sub>3</sub>** [Mn<sub>3</sub>L<sub>1,2</sub>(Cl)<sub>2</sub>] [L<sub>1</sub>=N1,N3-bis(3-methoxysalicylidene) diethylenetriamine] and **2-Mn<sub>3</sub>** [Mn<sub>3</sub>L<sub>2</sub>(C<sub>6</sub>H<sub>4</sub>O<sub>2</sub>)<sub>2</sub>] [L<sub>2</sub>=N1,N3-bis(3-salicylidene) diethylenetriamine] based on nitrogen-rich Schiff-base pentadentate ligands. The introduction of TG-MS (thermogravimetry associated with mass spectroscopy) explores the difference and universality of the pyrolysis mechanism of two trinuclear manganese clusters, and divides the pyrolysis process into three Areas (Area I/II/III) according to temperature. Combined with other character-

ization techniques, the materials in these three areas were analyzed to explain the effect of ligand modification on the electrochemical properties of cluster pyrolysis derivatives. It is found that the Area III derivatives have the best capacitance performance, when the current density is 1 A g<sup>-1</sup>, the specific capacitance of **1-900** is 1717 F g<sup>-1</sup>, and **2-900** is 350 F g<sup>-1</sup>. By comparison of the phase evolution process and electrochemical performance of the two manganese clusters, it is proposed that the crumbling of the molecular structure and stacking mode of trinuclear manganese clusters during pyrolysis will affect the capacitive properties of the derivatives. This work provides a guidance for the differences of the properties of pyrolytic derivatives under ligand modulation.

## Introduction

The main challenge of synthetic chemistry at present is to achieve the goal of precise synthesis, so as to achieve directional functional application.<sup>[1–6]</sup> In the well-known inorganic-organic hybrid material system, judicious and rational choice of ligands is an effective method to control the roadmap in precise synthesis.<sup>[7–9]</sup> The regulation of physicochemical properties of organometallic complex by ligand modulation has been reported that ligands can directly affect the properties of synthesized products.<sup>[10,11]</sup> However, the study of how the change of the ligand affects the function of the pyrolytic derivatives has rarely been explored. Although we have used the strategy of pyrolysis tracking to research and develop a variety of functional composite materials,<sup>[12,13]</sup> these works are all limited to one crystal, the direct impact of the different ligands on pyrolysis derivatives has not been studied in depth.

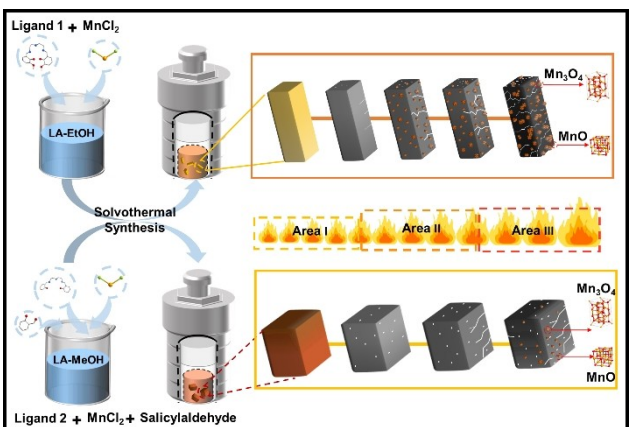
Our work system has considerable experience in the design, synthesis and function development of Schiff-base metal organic clusters (MOCs) based on o-vanillin.<sup>[14,15]</sup> For example, the MnO<sub>x</sub>/C nanocomposites with excellent capacitive properties prepared by pyrolysis of a salan-ligated manganese cluster.<sup>[16]</sup> Manganese oxide carbon matrix composites can be directly obtained by high temperature treatment of manganese based metal organic clusters, which can help manganese oxide break through its own limitations and achieve ideal capacitance performance.<sup>[17–19]</sup> However, the pyrolysis mechanism of Mn-based MOCs and its hierarchical phase evolution process still need to be further explored. Moreover, using chemical means to construct Mn-based MOCs with specified structure, and selecting different ligands to regulate the structure of Mn-based MOCs, then introducing pyrolysis means to explore the impact of different coordination environments on pyrolytic derivatives of Mn-based MOCs, which is conducive to establish a set of methodology for accurately synthesizing composites with specific functions guided by precursors and controlled by pyrolysis temperature.

In this work, we discuss the pyrolysis process of two trinuclear manganese clusters by similar ligand L<sub>1</sub> (N1, N3-bis(3-methoxysalicylidene) diethylenetriamine) and L<sub>2</sub> (N1, N3-bis(3-salicylidene) diethylenetriamine), meanwhile, the reasons for the differences in electrochemical properties of pyrolytic derivatives caused by ligand changes were clarified. The nitrogen-rich Schiff-base pentadentate ligands synthesized from o-vanillin and salicylaldehyde (Scheme 1) is selected not only because their considerable active sites provide more coordination opportunities for metal ions, but also the relatively rich nitrogen content will improve the nitrogen

[a] J. Li,<sup>+</sup> K. Zhao,<sup>+</sup> T. Li, Y. Shi, Dr. Y. Li, Dr. X. Peng  
Collaborative Innovation Center for Advanced Organic Chemical Materials  
Co-constructed by the Province and Ministry  
Ministry-of-Education Key Laboratory for the Synthesis and Application of  
Organic Functional Molecules  
College of Chemistry & Chemical Engineering  
School of Microelectronics  
Hubei University  
Wuhan, 430062 (P.R. China)  
E-mail: ybli@hubu.edu.cn  
pengxu@hubu.edu.cn

[+] These authors contributed equally to this work.

Supporting information for this article is available on the WWW under  
<https://doi.org/10.1002/batt.202200487>



**Scheme 1.** Synthetic route of **1-Mn<sub>3</sub>**/**2-Mn<sub>3</sub>** and preparation process of manganese oxide nitrogen doped carbon skeleton **1-T**/**2-T** via controlled pyrolysis. Color code: Mn orange; O red; N blue; Cl green; C gray.

doping of pyrolysis derivatives, which is benefit to boost the electrochemical properties of composites.<sup>[20,21]</sup> In order to pursue the universality of pyrolysis mechanism, TG-MS technology is introduced to analyze and compare the pyrolysis mechanisms of **1-Mn<sub>3</sub>** and **2-Mn<sub>3</sub>**. The properties of the derivatives were discussed by XRD, SEM/HRTEM, XPS, Raman and other characterization methods, then the reasons for the differences in capacitance performance of the derivatives were further explained. Finally, from the unique perspective of molecular structure and stacking way, the influence of the collapse mode of different trinuclear manganese clusters in the pyrolysis process on the capacitance performance of derivatives is expounded.

## Results and Discussion

The single-crystal X-ray diffraction (XRD) was utilized to identify the crystal structure of **1-Mn<sub>3</sub>** [ $\text{Mn}_3\text{L}_1(\text{Cl})_2$ ] [ $\text{L}_1 = \text{N}1, \text{N}3\text{-bis}(3\text{-methoxysalicylidene)}\text{ diethylenetriamine}$ ] and **2-Mn<sub>3</sub>** [ $\text{Mn}_3\text{L}_2(\text{C}_7\text{H}_4\text{O}_2)_2$ ] [ $\text{L}_2 = \text{N}1, \text{N}3\text{-bis}(3\text{-salicylidene)}\text{ diethylenetriamine}$ ]. The result shows that **1-Mn<sub>3</sub>** crystallizes in the monoclinic space group  $\text{C}2/\text{c}$  (Table S1 in Supporting Information). As a discrete neutral molecule, three Mn atoms in **1-Mn<sub>3</sub>**, are bridged and protected by two L1, a trinuclear Mn cluster structure unit similar to bowknot is formed by staggered twisting. There are two different hexa-coordinated modes of Mn (II) ions in clusters. One Mn ion in a hexa-coordination mode is located in the bowknot center which coordinated with four deprotonated phenol oxygens O2, O3 [Mn1–O2 = 2.2189(11) Å, Mn1–O3 = 2.0864(11) Å] and two deprotonated aldehyde oxygen O1 [Mn1–O1 = 2.3448(13) Å] to form a distorted octahedral configuration. Another Mn ion in a hexa-coordination mode is at both ends of the bowknot, in a nearly square pyramid geometry, equatorial plane is occupied by N1, N2, N3 [M2–N1 = 2.2859(14) Å, M2–N2 = 2.2718(16) Å, M2–N3 = 2.5350(17) Å] and deprotonated phenol oxygens O2, O3 [M2–O2 = 2.2108(11) Å, M2–O3 = 2.1450(11) Å], axial position is

occupied by a free Cl ion [M2–Cl1 = 2.4527(5) Å] (Figure S1 and Table S2). Meanwhile, **2-Mn<sub>3</sub>** is a neutral molecule crystallized in the monoclinic space group  $\text{P}2/n$  (Table S3). Three Mn (one Mn1, two Mn2) ions are protected by two L2 ligands and two salicylaldehyde ligands, in which Mn1 is located in the center and the other two Mn2 are located at two endpoints, respectively. The whole frame forms a trinuclear manganese cluster structural unit similar to a bowknot through staggered torsion. Among them, the Mn–O is between 2.0760–2.2143 Å and the Mn–N is between 2.233–2.385 Å. Mn2 forms a hexa-coordinated octahedral configuration with two O (O2, O3) on one coordinated salicylaldehyde, two O (O1, O4) and two N (N2, N3) on two L2. O2 on salicylaldehyde coordinated with Mn2  $\mu$ 2 is bridged with Mn1. O2 on another salicylaldehyde, N1 on two L2 and O1 on two L2 coordinated with Mn2 are also bridged with Mn1 to form a six coordinated octahedral configuration (Figure S4 and Table S4).

In order to figure out the pyrolysis mechanism of **1-Mn<sub>3</sub>** and **2-Mn<sub>3</sub>**, we initially adopted thermogravimetry (TG) to explore the weight change of them with temperature (Figure 1a and d), subsequently associated with mass spectroscopy (TG-MS), according to the detected escaped molecular fragments (Figure 1b and e).

The pyrolysis process of **1-Mn<sub>3</sub>** can be accurately deduced in three stages (Figure 1c). I) In the temperature range of 250–450 °C, fragments of  $\text{CH}_3^+$  ( $m/z = 15$ ),  $\text{CH}=\text{N}^+$  ( $m/z = 27$ ),  $\text{Cl}^+$  ( $m/z = 35$ ),  $\text{CH}_2\text{NHCH}_2^+$  ( $m/z = 42$ ) and  $\text{CH}_3\text{Cl}^+$  ( $m/z = 50$ ) were detected. There are two sources of  $\text{CH}_3^+$ , one is from the fragmentation of ligand directly, the other is from further cracking of  $\text{CH}_2\text{NHCH}_2^+$  into  $\text{CH}_2^+$  and  $\text{CH}=\text{N}^+$ , which also explains the  $\text{CH}=\text{N}^+$  source in this temperature period, and the  $\text{CH}_2\text{NHCH}_2^+$  re-cracking situation continued until about 450 °C. Meanwhile,  $\text{CH}_3\text{Cl}^+$  was formed by the combination of  $\text{CH}_3^+$  and  $\text{Cl}^-$ , where  $\text{Cl}^-$  was dropped directly from the ligand. II) In the temperature range of 450–550 °C,  $\text{CH}_3^+$  and  $\text{CH}=\text{N}^+$  fragments were detected again. Interestingly, the peak intensity of  $\text{CH}_3^+$  and  $\text{CH}=\text{N}^+$  reflected a relation of "as one falls, another rises". The peak intensity of  $\text{CH}_3^+$  increased at first and then decreased, which due to the split out  $\text{CH}_3^+$  from exposed  $\text{CH}_2\text{N}=\text{CH}^+$ . By contrary, when the temperature continues to 500 °C, the peak intensity of  $\text{CH}=\text{N}^+$  first decreased and then increased, which may be caused by the shedding of  $\text{CH}=\text{N}^+$  from exposed N-containing sites after 500 °C. III) With temperature constantly raise, the structure of **1-Mn<sub>3</sub>** completely collapses to form the nitrogen-doped carbon matrix eventually.

The pyrolysis process of **2-Mn<sub>3</sub>** can also be divided into three stages (Figure 1f). I) before 300 °C,  $\text{CH}_3\text{OH}^+$  ( $m/z = 31$ ) fragment was detected, which indicates the volatilization of solvent molecules. II) The temperature range of 300–800 °C still can be subdivided into two sections for analysis.  $\text{CH}_3^+$  ( $m/z = 15$ ),  $\text{CH}=\text{N}^+$  ( $m/z = 27$ ) and  $\text{CH}_2\text{NHCH}_2^+$  ( $m/z = 43$ ) fragments were detected in the temperature range of 300–450 °C, which comes as a result of  $\text{CH}_2\text{NHCH}_2^+$  fell from the ligand initially then split into  $\text{Cl}^+$  and  $\text{CH}=\text{N}^+$ , the re-split of  $\text{CH}_2\text{NHCH}_2^+$  terminates about 450 °C. The peak intensity of  $\text{CH}_3^+$  and  $\text{CH}=\text{N}^+$  fragments detected in the temperature range of 450–800 °C also appear a phenomenon of "as one falls, another

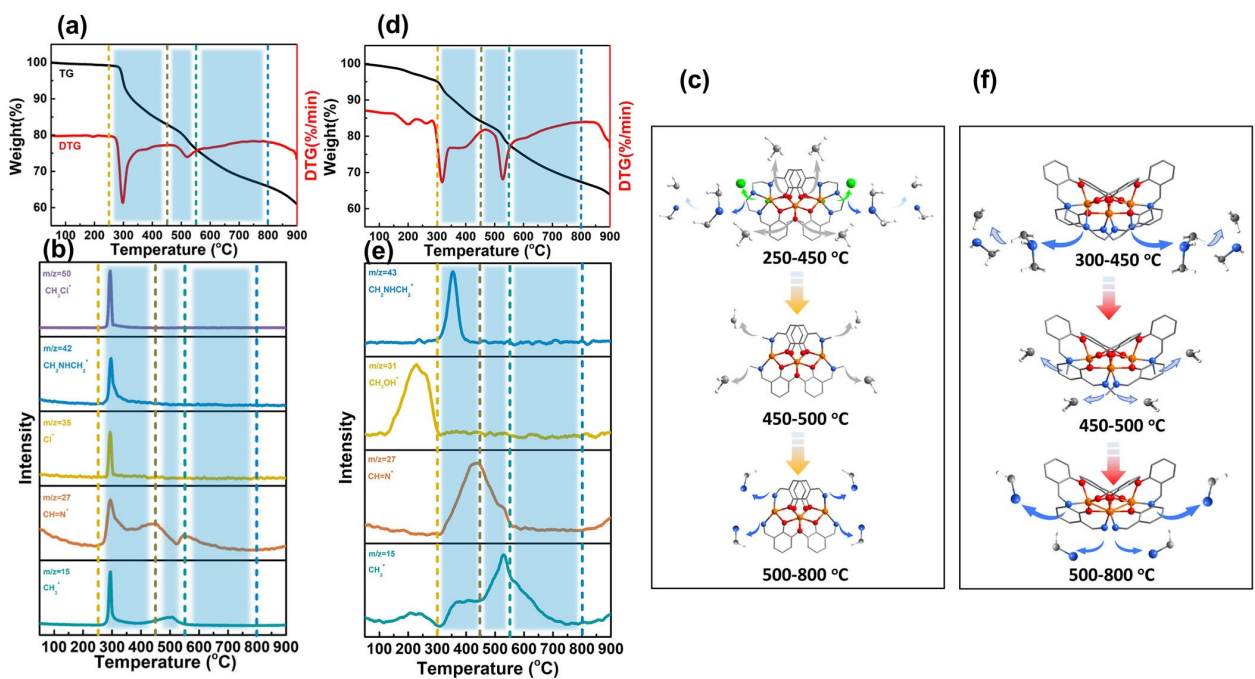


**Figure 1.** Evolution process elucidation. a) TG-DTG of **1-Mn<sub>3</sub>**. b) Main gaseous molecule detected by TG-MS during the Pyrolysis process of **1-Mn<sub>3</sub>**. c) Possible illustration of pyrolysis evolution process of **1-Mn<sub>3</sub>**. d) TG-DTG of **2-Mn<sub>3</sub>**. e) Main gaseous molecule detected by TG-MS during the Pyrolysis process of **2-Mn<sub>3</sub>**. f) Possible illustration of pyrolysis evolution process of **2-Mn<sub>3</sub>**.

rises" which ascribe to the splitting decomposition of  $\text{CH}_3^+$  and  $\text{CH}=\text{N}^+$  from exposed  $\text{CH}_2\text{N}=\text{CH}$  successively. III) after 800 °C, the structure of **2-Mn<sub>3</sub>** crumble entirely and turn into the nitrogen-doped carbon matrix.

Hence, in accordance with the similarities and differences in the TG/TG-MS analysis of **1-Mn<sub>3</sub>** and **2-Mn<sub>3</sub>**, we divide the entire pyrolysis process into three distinct areas: (Area I) Low-temperature area, Room-temperature to 500 °C; (Area II) Transition-decomposition-recombination temperature area: 500–800 °C; (Area III) High-temperature area: after 800 °C.

The research of phase transformation in the pyrolysis process at the macroscopic level help us understand the changes of molecular structure at the microscopic scale. Therefore, powder X-ray diffraction (PXRD) and scanning electron microscopy (SEM) were conducted to explore the composition and surface topography of **1-T** and **2-T**. In the integral pyrolysis process, their phase identification both underwent a transition from crystalline to amorphous and then to the new crystalline state (Figure 2a). It is worth noting that in Area II and Area III, they have distinct diffraction peaks at the same position. The diffraction peaks at 34.9°, 40.5°, 58.7°, 70.1° and 73.8° can be indexed to (111), (200), (220), (311) and (222) planes of MnO (JCPDS card No. 07-0230), respectively. The diffraction peaks at the positions of 18.0°, 28.8°, 32.3°, 36.0°, 44.4°, 59.8°, 64.6° and 77.5° are successively attributed to the (101), (112), (103), (211), (220), (224), (400) and (404) planes of  $\text{Mn}_3\text{O}_4$  (JCPDS card No. 24-0734), respectively. This illustrates that the new phase formed in Area II and Area III is MnO and  $\text{Mn}_3\text{O}_4$ . SEM images reveal the morphologic transformation of

**1-T** and **2-T** (Figure 2b). For **1-T**, it is clearly that with the increase of pyrolysis temperature, the cracks on the surface of derivants become deeper. In Area II and Area III, cubic or octahedral manganese oxide particles can be observed and uniformly dispersed on the surface and gap of carbon matrix, which is consistent with the results obtained from XRD. As the further increase of pyrolysis temperature, the agglomeration of manganese oxide particles is accelerated and the carbon matrix pores increase significantly. It's worth saying that, the undue agglomeration of manganese oxides may hinder the ion/electron transfer process and reduce the material utilization.<sup>[22]</sup> **2-T** is different, although the derivates surface still cracks gradually with the increase of temperature, only in Area III can observe a small amount of cubic manganese oxide particles distributed over the surface and gap of carbon matrix, this may be because the manganese oxide particles formed before Area III are covered in carbon matrix, which is not conducive to the generation of pseudocapacitance.<sup>[23]</sup> The high-angle annular dark-field (HAADF) and mapping of **1-900** (Figure 3a and b) and **2-900** (Figure 3d and e) also showed the  $\text{MnO}_x$  particles with size about 50–100 nm are uniformly dispersed in carbon matrix. In addition, the high-resolution transmission electron microscopy (HRTEM) was used to verify the phase composition. For **1-900**, the lattice fringes with lattice spacing of 0.255 nm and 0.489 nm can be clearly observed (Figure 3c), which correspond to the planes of MnO (111) and  $\text{Mn}_3\text{O}_4$  (101). In **2-900**, obvious lattice fringes with spacing of 0.289 nm and 0.493 nm were observed (Figure 3f), corresponding to MnO (200) and  $\text{Mn}_3\text{O}_4$  (101) planes. These analyses point that the

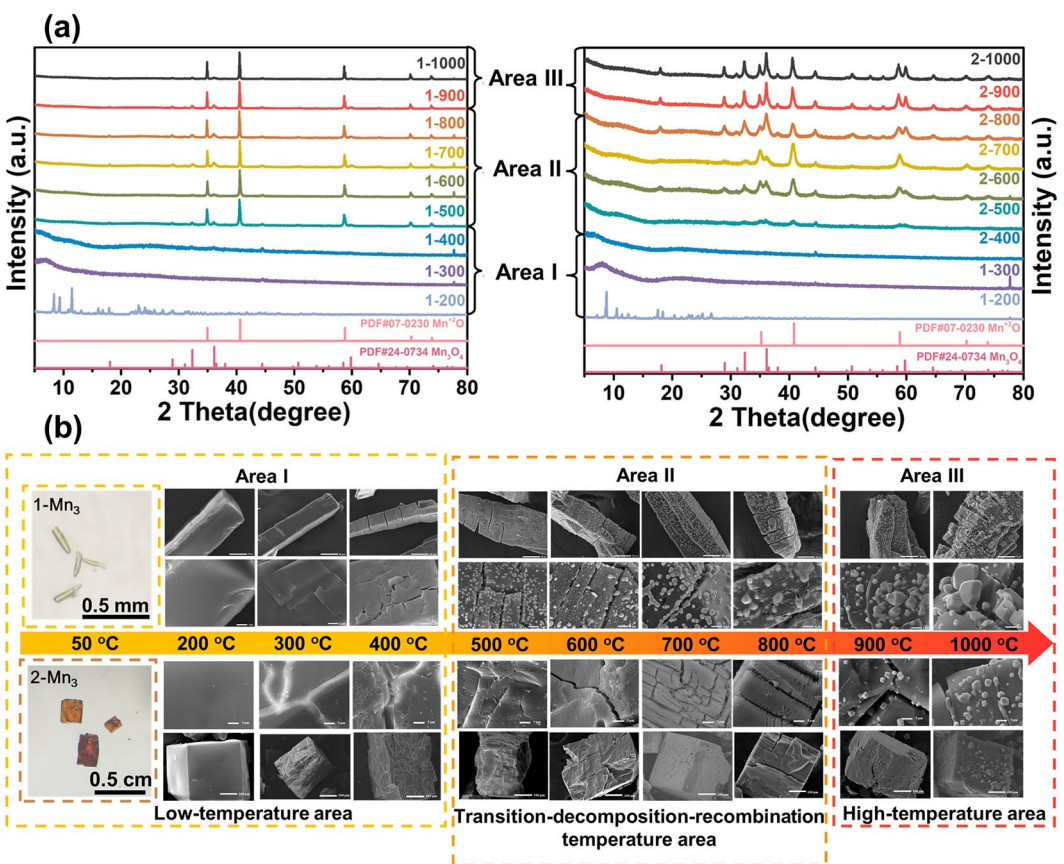
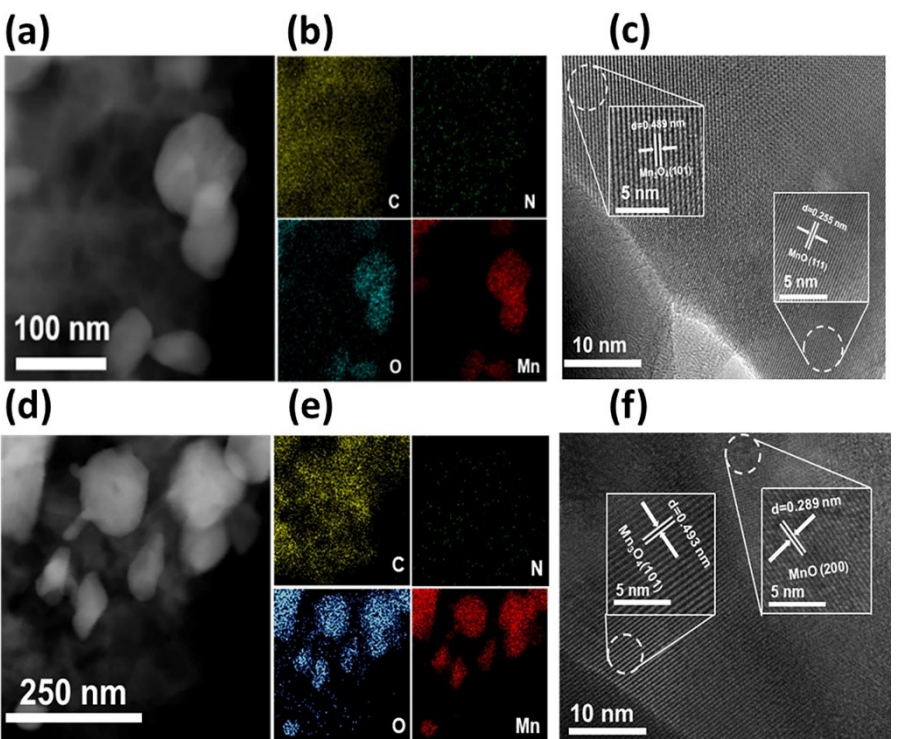


Figure 2. Comparison of morphology evolution of two Mn<sub>3</sub> clusters. a) XRD patterns of 1-T and 2-T. b) Microscopy images of 1-T and 2-T.

derivatives in Area II/III of 1-T and 2-T are actually N-doped carbon matrix with manganese oxides embedded (MnO<sub>x</sub>@NC).

For acquainting the chemical composition and valence state of MnO<sub>x</sub>@Cs, X-ray photoelectron spectroscopy (XPS) was introduced to analyze the 1-T and 2-T surface in Area II/III. Both full-survey-scan XPS spectrum shows that the main peaks appeared at 83.0, 285.0, 400.0, 532.0 and 642.0 eV, which are assigned to Mn 3 s, C 1s, N 1s, O 1s, and Mn 2p, respectively (Figure 4a and b). It is worth mentioning that the energy separation between the two peaks of Mn 3 s is related to the mean manganese oxidation state, which shows a certain inverse liner correlation.<sup>[24]</sup> In other words, the mean valence state of manganese oxidation can be judged by the difference between the two peaks of Mn 3 s, and then the relative proportion of each valence state can be determined.<sup>[25]</sup> With regard to all samples in Area II/III of 1-T and 2-T, the difference between the two peaks of Mn 3 s decreases successively. For 1-T, the corresponding mean valence states of manganese can be calculated as 2.17, 2.22, 2.30, 2.33, 2.56 and 2.65, respectively (Figure S7). As for 2-T, those values in the corresponding area are 2.05, 2.09, 2.32, 2.39, 2.42 and 2.54 (Figure S12). Further observation of their high-resolution Mn 2p shows two important peaks, in which the bonding energy of Mn 2p<sub>3/2</sub> is 640.9 eV, Mn 2p<sub>1/2</sub> is 652.8 eV, both can be attributed to Mn<sup>2+</sup>, another pair of peaks appeared at 642.1 eV and 653.7 eV, all can be attributed to Mn<sup>3+</sup>. The ratio of Mn<sup>2+</sup>/

Mn<sup>3+</sup> can be obtained by semi quantitative analysis according to the peak area, based on Mn<sup>2+</sup>/Mn<sup>3+</sup> ratio, the average valence state of Mn are deduced.<sup>[26]</sup> For 1-T, calculated manganese average state are as follows: 2.15, 2.19, 2.28, 2.36, 2.57 and 2.62 (Figure S8). As for 2-T, the calculated values are 2.04, 2.11, 2.30, 2.41, 2.44 and 2.51 (Figure S13). Those results are highly consistent with the mean valence state calculated by the difference between the peaks of Mn 3s. Therefore, it is evident to infer that the proportion of Mn<sub>3</sub>O<sub>4</sub> is enhanced in the wake of promoting pyrolysis temperature. It was reported earlier that the appearance of Mn<sub>3</sub>O<sub>4</sub> is beneficial to strengthen the storage capacity of the composites.<sup>[27]</sup> Moreover, their high resolution N 1s spectrum is convoluted into three peaks: pyridinic N (398.5 eV), pyrrolic N (399.8 eV) and graphitic N (401.1 eV) (Figures S11 and S16). In previous report, the particular bonding mode of pyridinic N and pyrrolic N can introduce more electrons into the system to improve the conductivity, and the nitrogen-containing carbon defects as the electrochemical active sites would heighten the capacitance performance of the materials.<sup>[28,29]</sup> Meanwhile, three peaks of Mn–O (529.8 eV), oxygen defect (531.6 eV) and C–O (533.1 eV) were fitted by the high resolution O 1s spectrum (Figures S10 and S15). Additionally, the high-resolution C 1s spectrum show three different types of N species: sp<sup>2</sup> C (284.8 eV), C–O or C–N (285.7 eV), and C=O or C=O (288.9 eV) (Figures S9 and S14).



**Figure 3.** a) HAADF image, b) Elemental mapping images, c) HRTEM images of 1-900. d) HAADF image, e) Elemental mapping images, and f) HRTEM images of 2-900.

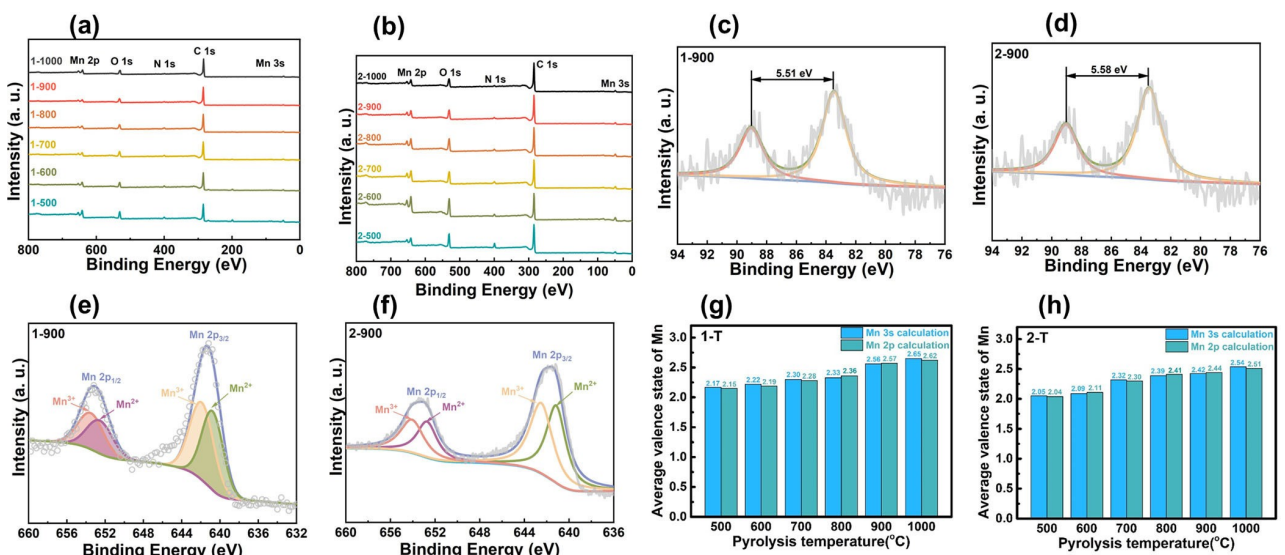


**Figure 4.** XPS survey spectra of a) 1-T and b) 2-T. XPS spectrum for Mn 3 s of c) 1-900 and d) 2-900. XPS spectrum for Mn 2p of e) 1-900 and f) 2-900. Average valence state of Mn calculated based on Mn 3 s and Mn 2p: g) 1-T, h) 2-T.

Raman spectroscopy analyzes the degree of graphitization for 1-T and 2-T in Area II/III (Figure 5a and b). Except 2-500 two obvious characteristic peaks of carbon materials arise in the spectrum of leftover samples, which are defective carbon (D-band) located at  $1338.9\text{ cm}^{-1}$  and graphite carbon (G-band) located at  $1595.8\text{ cm}^{-1}$ . D-band corresponds to disordered

carbon or defective graphite structure, while G-band is the characteristic of graphite layer.<sup>[30]</sup> Therefore, the ratio of peak intensity  $I_D/I_G$  reflects the disorder degree of graphite. For 1-T in Area II, the ratio increases from 0.81 to 0.93, which indicates that the defects change incessantly with pyrolysis temperature. In Area III, the ratio remains at maximum value of 0.95, which

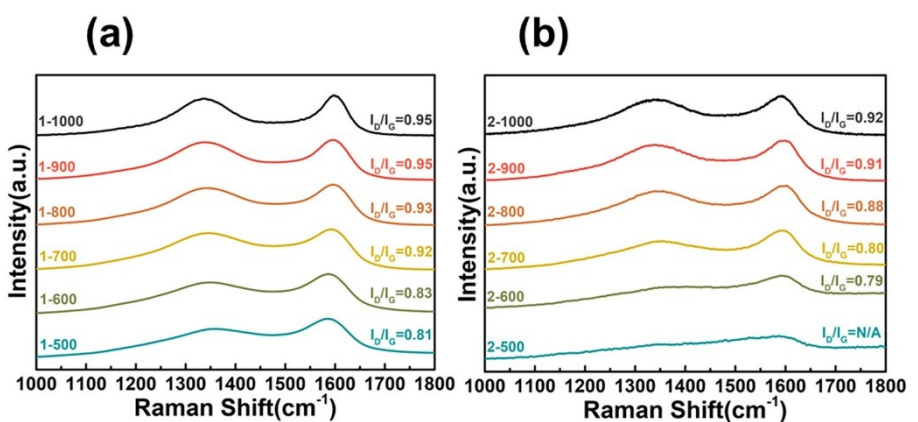


Figure 5. Raman spectroscopy of a) 1-T and b) 2-T.

means that a stable carbon skeleton structure is formed in those samples. As for 2-T in Area II/III, the ratio of  $I_D/I_G$  increases from 0.79 to 0.92. According to what we are informed, the introduction of defects can change the physical and chemical properties of carbon based materials, affect the density and activity of surface active sites, and improve the overall electrochemical performance of carbon based materials.<sup>[31]</sup> Moreover, the surface area and pore size distribution of the composites affect the transmission efficiency of ions and electrons, which is also the key factor to determine the capacitance of the prepared electrodes.<sup>[32,33]</sup>

The samples in Area II/III of 1-T and 2-T were selected to evaluate their surface area and pore size distribution by measuring the nitrogen adsorption desorption isotherm. In 1-T,

the adsorption-desorption isotherm of 1-500 is similar to Type II, the adsorption capacity is quite low, which is a typical physical adsorption process on non-porous or macroporous materials, other samples exhibited Type IV adsorption-desorption isotherms, which increased sharply at low relative pressure, reflecting the microporous filling phenomenon, meanwhile H4 adsorption hysteresis loop appeared in the medium pressure region, which is a typical mesoporous adsorption characteristic (Figure 6a). Then corresponding pore size distribution is calculated by nitrogen desorption branch DFT method (Figure 6c). Except 1-500, the pore size distribution of other samples is mainly concentrated in two ranges: micropores of 0.5–2 nm and mesopores greater than 2 nm. This indicates that there are micropores and mesopores in the sample after 600 °C,

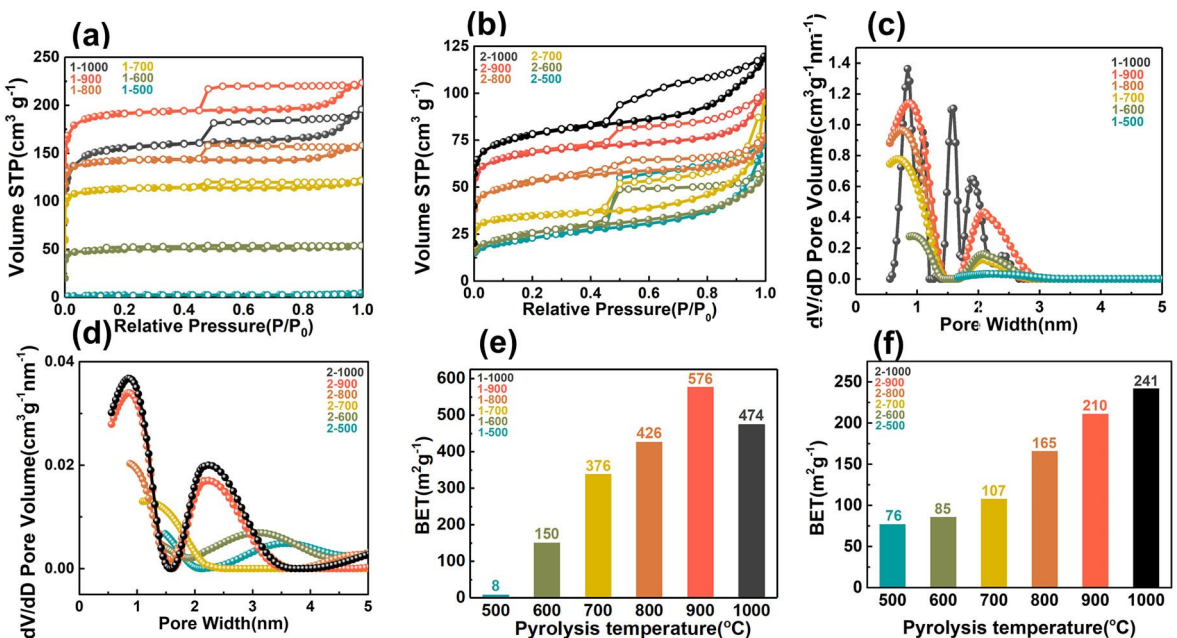
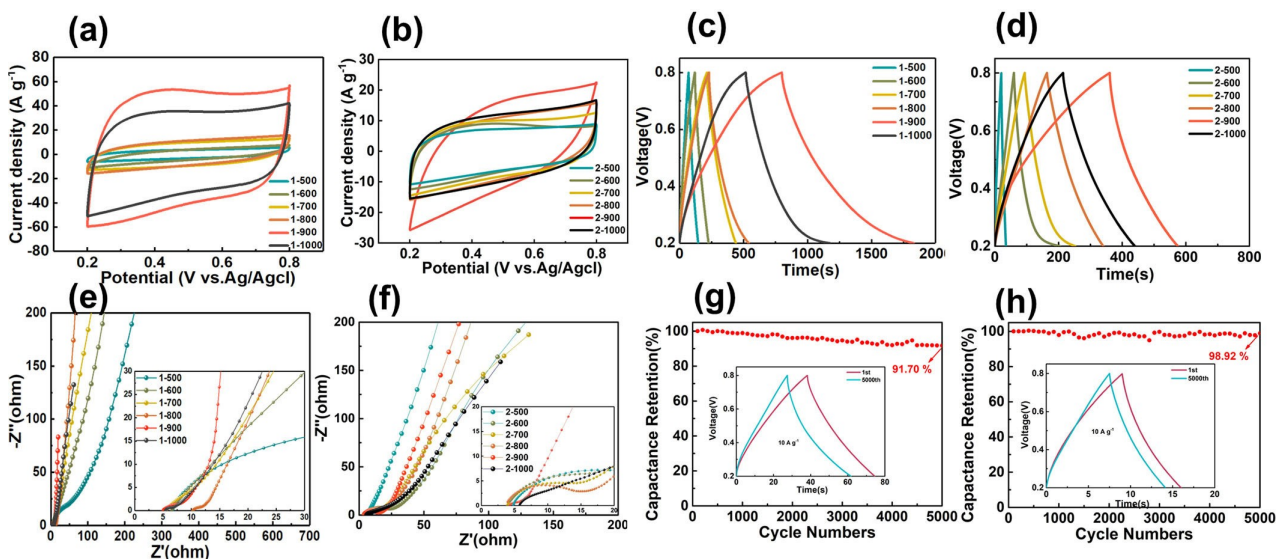


Figure 6.  $N_2$  adsorption iso-thermals of a) 1-T and b) 2-T. Micropore size distributions of c) 1-T and d) 2-T. Brunauer-Emmett-Teller (BET) results of e) 1-T and f) 2-T.

which is conducive to the improvement of capacitance.<sup>[34]</sup> It is noted that micropores can effectively trap ions for high energy storage, whereas the mesoporous can accelerate the kinetic process of the ion diffusion in the electrodes, and a well balance between micropores and mesopores can maximize capacitance.<sup>[35]</sup> Based on Brunauer Emmett Teller (BET) calculations, the specific surface areas of 1-500, -600, -700, -800, -900 and -1000 could be obtained (Figure 6e), respectively, they are 8, 150, 376, 426, 576 and 474 m<sup>2</sup>g<sup>-1</sup>. Obviously, BET surface area of 1-900 is the largest, and the total pore volume reaches 0.35 cm<sup>3</sup>g<sup>-1</sup>. As for 2-T, all samples exhibited Type IV adsorption-desorption isotherms (Figure 6b). Based on DFT calculation obtained corresponding pore size distribution. The pore size distribution of all samples is mainly concentrated in two ranges: micropores of 0.5-2 nm and mesopores greater than 2 nm (Figure 6d). The specific surface areas of 2-500, -600, -700, -800, -900 and -1000 are as follow: 76, 85, 107, 165, 210, 241 m<sup>2</sup>g<sup>-1</sup>, which were obtained by BET calculation (Figure 6f). According to those characterization analysis, we believe that their samples in Area III has potential as supercapacitor electrode.

To verify our thoughts, we further test the electrochemical performance of 1-T and 2-T in Area II/III. In three-electrode system, cyclic voltammetry (CV) and constant current charge and discharge (GCD), electrochemical impedance spectroscopy (EIS) measurements were taken to test the electrode materials which were prepared by them. The CV curves of 1-T (Figure 7a) electrodes at 100 mVs<sup>-1</sup> was tested within the potential window of 0.2–0.8 V.<sup>[36]</sup> It can be clearly observed that the integral area of CV curve of 1-900 electrode is much larger than that of others, indicating it has high capacitance. Correspondingly, in the GCD curves (Figure 7c) measured at 1 Ag<sup>-1</sup>, the discharge time of the 1-900 electrode is much longer than that of others, which is consistent with the results obtained from

the CV curves. Substituting the data which acquired form GCD curves into given formula, through calculation, 1-900 contains the maximum specific capacitance and up to 1717 Fg<sup>-1</sup>. This value records the best value as a manganese oxide material derived from MOF (Table S5). At the same time, as shown in the EIS curves of 1-T (Figure 7e), the charge transfer resistance of 1-900 is the lowest, which is only 1.46 Ω, in the frequency range from 100 kHz to 100 mHz. Individually test CV curves of 1-900 electrode in the range of 5–200 mVs<sup>-1</sup> at different scanning rate, the shape of CV curves are similar to rectangle and does not transform with the change of sweep rate, reveals the rapid charge-discharge dynamics characteristics and approximately ideal capacitive behavior of 1-900. Furthermore, the GCD curves of electrode which named 1-900 was measured under different current densities in the range of 1–20 Ag<sup>-1</sup>, those curves are typical triangles, following the formula, when the current density is 20, 10, 5, 2 and 1 Ag<sup>-1</sup>, the specific capacitance values are 410, 603, 728, 1040 and 1717 Fg<sup>-1</sup>, respectively (Figure S18). Besides that, stability is also an essential factor to evaluate the practicality of supercapacitor electrodes. The excellent cycle life of 1-900 makes it still have 91.70% capacitance retention even after 5000 charge discharge cycles (Figure 7g) which indicates it has outstanding cycle stability as a supercapacitor electrode. The capacitance performance of 2-T is tested under the same test conditions and parameters of 1-T. In the CV Curve of 2-T (Figure 7b), 2-900 has the largest integral area. The corresponding GCD curves shows that 2-900 has the longest charge discharge time (Figure 7d), the specific capacitance of 2-900 is 356 Fg<sup>-1</sup> after calculation. It can be seen from the EIS curve of 2-T (Figure 7f) that the charge transfer resistance of 2-900 is the smallest. After 5000 charge/discharge cycles (Figure 7h), the capacitance retention of 2-900 is as high as 98.92%.



**Figure 7.** Supercapacitor behaviors of 1-Mn<sub>3</sub> and 2-Mn<sub>3</sub> clusters are compared. CV curves of a) 1-T and b) 2-T electrodes at 100 mVs<sup>-1</sup>, GCD curves of c) 1-T and d) 2-T electrodes at 1 Ag<sup>-1</sup>. Comparison of the electrochemical impedance spectroscopy (EIS) for e) 1-T and f) 2-T electrodes. Capacitance retention of g) 1-900 and h) 2-900 electrodes over 5000 charge/discharge cycles.

It is worth noting that, the capacitance properties of the two kinds of pyrolysis derivatives 1-T and 2-T obtained under same experimental conditions are totally different. We have reason to believe this difference is caused by specific precursor with various ligands. Hence, we compared the molecular structure and stacking mode of **1-Mn<sub>3</sub>** and **2-Mn<sub>3</sub>** (Figure 8). In terms of molecular structure, the uncoordinated methoxy groups in **1-Mn<sub>3</sub>** are located at the periphery of the coordination structure, once the temperature reaches the threshold, manganese will form manganese oxide with oxygen and deembed from the ligand structure, there are also two chlorine coordinated with manganese at the periphery of the ligand structure, the fracture of Mn–Cl during pyrolysis will make manganese become the active center, which is conducive to the formation of manganese oxide. All oxygen in **2-Mn<sub>3</sub>** participates in the coordination of manganese are embedded into the coordination center, when the temperature threshold is reached, the formed manganese oxide will be wrapped by the ligand structure. In terms of stacking mode, the molecular arrangement of **1-Mn<sub>3</sub>** is planar, the carbon substrate formed after the collapse of ligand structure during pyrolysis will be loaded with manganese oxide, which is benefit to the pseudo-capacitance energy storage of composite materials. The molecular arrangement of **2-Mn<sub>3</sub>** is arched and staggered, the

carbon substrate formed by the collapse of ligand structure during pyrolysis will be covered with manganese oxide, that will hinder the generation of pseudo-capacitance.

## Conclusion

In conclusion, we proposed a pair of trinuclear manganese clusters **1-Mn<sub>3</sub>** and **2-Mn<sub>3</sub>** based on the nitrogen rich Schiff base pentadentate ligand L1 and L2, L1 and L2 are obtained by aldol condensation of o-vanillin/salicylaldehyde and diethylenetriamine respectively, and different MnO<sub>x</sub>/C nanostructures are prepared after pyrolysis process. The pyrolysis process of the two trinuclear manganese clusters was tracked by TG-MS technology, which compared the difference and similarity of their pyrolysis mechanism, and divided into three Areas: (Area I) with the removal of anions and solvent molecules, the ligand structure began to collapse; (Area II) the ligand structure is transformed to carbon skeleton, and metal oxides begin to form; (Area III) the composites tend to be stable to form hierarchical nanostructures. XRD, HRTEM, XPS, Raman and BET characterization were used to further analyze their hierarchical evolution in the pyrolysis process, explaining the excellent capacitance performance of derivative in Area III. **1-900** not only has a reasonable pore size distribution which promotes electron transfer and transport, but also has good reversibility due to the ratio of Mn<sup>2+</sup> to Mn<sup>3+</sup> was about 1:1, when the current density is 1 A g<sup>-1</sup>, the specific capacitance of **1-900** is 1717 F g<sup>-1</sup>, and **2-900** is 350 F g<sup>-1</sup>. It is the first time to study the influence of the collapse way of two similar ligands trinuclear manganese clusters during pyrolysis on the capacitive properties from the unique perspective of molecular structure and stacking mode. We believe that this work will realize the complete unity from the top-design of ligand modulation to the bottom-logic of pyrolytic derivative application.

## Experimental Section

### Synthesis of **1-Mn<sub>3</sub>** ( $[\text{Mn}_3\text{L}_1_2(\text{Cl})_2]$ [ $\text{L}_1 = \text{N}_1$ , N3-bis(3-methoxysalicylidene)])

At room temperature, in an autoclave with a capacity of 25 mL, 20 mL absolute ethanol was added as solvent, and then L1 (1.0 mmol, 0.371 g) and was dissolved in the solvent to form yellow transparent solution, subsequently added MnCl<sub>2</sub>·4H<sub>2</sub>O (1.0 mmol, 0.198 g) and 0.45 mL of triethylamine into the mixed liquor under stirring condition. The reaction vessel was sealed and set in a 100°C oven for 48 h, after the reaction, yellow cuboid **1-Mn<sub>3</sub>** were formed. Finally, washed **1-Mn<sub>3</sub>** with ethanol and natural dried. Yield (based on Mn): 41.3%.

### Synthesis of **2-Mn<sub>3</sub>** ( $[\text{Mn}_3\text{L}_2_2(\text{C}_7\text{H}_4\text{O}_2)_2]$ [ $\text{L}_2 = \text{N}_1$ , N3-bis(3-salicylidene) diethylenetriamine])

At room temperature, in an autoclave with a capacity of 25 mL, 20 mL absolute methanol was added as solvent, and then L2 (1.0 mmol, 0.309 g) and salicylaldehyde (1.0 mmol, 0.122 g) was

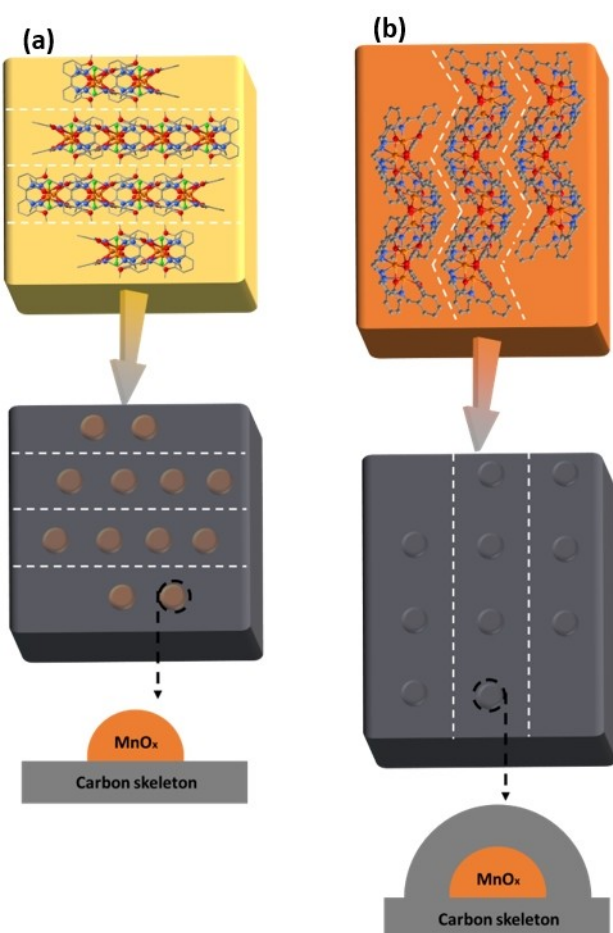


Figure 8. Collapse mode during pyrolysis of a) **1-Mn<sub>3</sub>** and b) **2-Mn<sub>3</sub>**.

dissolved in the solvent to form an orange transparent solution, subsequently added  $\text{MnCl}_2 \cdot 4\text{H}_2\text{O}$  (1.0 mmol, 0.198 g) and 0.45 mL of triethylamine into the mixed liquor under stirring condition. The reaction vessel was sealed and set in a 100 °C oven for 48 h, after the reaction, orange cuboid 2-Mn<sub>3</sub> were formed. Finally, washed 2-Mn<sub>3</sub> with methanol and natural dried. Yield (based on Mn): 53.8%.

## Materials

This material is available free of charge via the Internet at <http://pubs.acs.org>. Figures S1–S3, Tables S1 and S2 and Figures S7–S11, show the structure, PXRD of the 1-Mn<sub>3</sub>, and XPS high-resolution Mn 3 s, Mn 2p, C 1s, O 1s, N 1s peaks of 1-T. Figures S17(a) shows total pore volume values of 1-T. Figures S18(a) shows GCD curves of 1-T electrode at different current densities. Figures S4–S6, Tables S3 and S4 and Figures S12–S16 show the structure, PXRD of the 2-Mn<sub>3</sub>; and XPS high-resolution Mn 3 s, Mn 2p, C 1s, O 1s, N 1s peaks of 2-T. Figures S17(b) shows total pore volume values of 2-T.

## Conflict of Interest

The authors declare no conflict of interest.

## Data Availability Statement

The data that support the findings of this study are available from the corresponding author upon reasonable request.

**Keywords:** This work was financially supported by the NSFC of Hubei (Grants 2021CFB420).

- [1] X. Wang, J. Zhuang, Q. Peng, Y. Li, *Nature* **2005**, *437*, 121–124.
- [2] C. Sun, B. K. Teo, C. Deng, J. Lin, G.-G. Luo, C.-H. Tung, D. Sun, *Coord. Chem. Rev.* **2021**, *427*, 213576.
- [3] Z. Song, G. Zhang, X. Deng, Y. Tian, X. Xiao, W. Deng, H. Hou, G. Zou, X. Ji, *Adv. Funct. Mater.* **2022**, *32*.
- [4] Z. Song, G. Zhang, X. Deng, K. Zou, X. Xiao, R. Momen, A. Massoudi, W. Deng, J. Hu, H. Hou, G. Zou, X. Ji, *Nano-Micro Lett.* **2022**, *14*, 53.
- [5] X. Sun, L. Sun, G. Li, Y. Tu, C. Ye, J. Yang, J. Low, X. Yu, J. H. Bitter, Y. Lei, D. Wang, Y. Li, *Angew. Chem. Int. Ed.* **2022**, *61*, e202207677.
- [6] T. Cui, Y.-P. Wang, T. Ye, J. Wu, Z. Chen, J. Li, Y. Lei, D. Wang, Y. Li, *Angew. Chem. Int. Ed.* **2022**, *61*, e202115219.
- [7] Z. Yin, Y.-L. Zhou, M.-H. Zeng, M. Kurmoo, *Dalton Trans.* **2015**, *44*, 5258–5275.
- [8] S.-Y. Liu, J.-P. Zhang, X.-M. Chen, *Cryst. Growth Des.* **2017**, *17*, 1441–1449.
- [9] J. Meng, X. Liu, C. Niu, Q. Pang, J. Li, F. Liu, Z. Liu, L. Mai, *Chem. Soc. Rev.* **2020**, *49*, 3142–3186.

- [10] M. Guo, H. Li, Y. Ren, X. Ren, Q. Yang, C. Li, *ACS Catal.* **2018**, *8*, 6476–6485.
- [11] X. Ma, H. Liu, W. Yang, G. Mao, L. Zheng, H.-L. Jiang, *J. Am. Chem. Soc.* **2021**, *143*, 12220–12229.
- [12] J.-Q. Zhao, D. Cai, J. Dai, M. Kurmoo, X. Peng, M.-H. Zeng, *Sci. Bull.* **2019**, *64*, 1667–1674.
- [13] Y.-F. Wang, Y. Liang, Y.-F. Wu, J. Yang, X. Zhang, D. Cai, X. Peng, M. Kurmoo, M.-H. Zeng, *Angew. Chem. Int. Ed.* **2020**, *59*, 13232–13237; *Angew. Chem.* **2020**, *132*, 13334–13339.
- [14] B. Pan, X. Peng, Y. Wang, Q. An, X. Zhang, Y. Zhang, T. S. Teets, M.-H. Zeng, *Chem. Sci.* **2019**, *10*, 4560–4566.
- [15] Q. An, B. Pan, L. Li, X. Peng, M.-H. Zeng, *Chin. J. Chem.* **2021**, *39*, 2529–2535.
- [16] X. Zhang, K. Zhao, X. Peng, M. Kurmoo, M.-H. Zeng, *Nano Res.* **2022**, *15*, 346–351.
- [17] Y. Hu, Y. Wu, J. Wang, *Adv. Mater.* **2018**, *30*, 1802569.
- [18] L. Peng, X. Peng, B. Liu, C. Wu, Y. Xie, G. Yu, *Nano Lett.* **2013**, *13*, 2151–2157.
- [19] N. Yu, K. Guo, W. Zhang, X. Wang, M.-Q. Zhu, *J. Mater. Chem. A* **2017**, *5*, 804–813.
- [20] B. Naskar, R. Modak, D. K. Maiti, M. G. B. Drew, A. Bauzá, A. Frontera, C. Das Mukhopadhyay, S. Mishra, K. Das Saha, S. Goswami, *Dalton Trans.* **2017**, *46*, 9498–9510.
- [21] J. Andrez, V. Guidal, R. Scopelliti, J. Pécaut, S. Gambarelli, M. Mazzanti, *J. Am. Chem. Soc.* **2017**, *139*, 8628–8638.
- [22] X. Zhang, Y. Zhu, A. M. Bruck, L. M. Housel, L. Wang, C. D. Quilty, K. J. Takeuchi, E. S. Takeuchi, A. C. Marschilok, G. Yu, *Energy Storage Mater.* **2019**, *19*, 439–445.
- [23] K. Lan, L. Liu, J.-Y. Zhang, R. Wang, L. Zu, Z. Lv, Q. Wei, D. Zhao, *J. Am. Chem. Soc.* **2021**, *143*, 14097–14105.
- [24] X. Peng, Y. Guo, Q. Yin, J. Wu, J. Zhao, C. Wang, S. Tao, W. Chu, C. Wu, Y. Xie, *J. Am. Chem. Soc.* **2017**, *139*, 5242–5248.
- [25] Y. Guo, Y. Tong, P. Chen, K. Xu, J. Zhao, Y. Lin, W. Chu, Z. Peng, C. Wu, Y. Xie, *Adv. Mater.* **2015**, *27*, 5989–5994.
- [26] D. Rangappa, K. D. Murukanahally, T. Tomai, A. Unemoto, I. Honma, *Nano Lett.* **2012**, *12*, 1146–1151.
- [27] Y. Chu, L. Guo, B. Xi, Z. Feng, F. Wu, Y. Lin, J. Liu, D. Sun, J. Feng, Y. Qian, S. Xiong, *Adv. Mater.* **2018**, *30*, 1704244.
- [28] T. Lin, I. W. Chen, F. Liu, C. Yang, H. Bi, F. Xu, F. Huang, *Science* **2015**, *350*, 1508–1513.
- [29] G. Ćirić-Marjanović, I. Pašti, S. Mentus, *Prog. Mater. Sci.* **2015**, *69*, 61–182.
- [30] F. Zheng, Y. Yang, Q. Chen, *Nat. Commun.* **2014**, *5*, 5261.
- [31] D. Xue, H. Xia, W. Yan, J. Zhang, S. Mu, *Nano-Micro Lett.* **2020**, *13*, 5.
- [32] C. Young, J. Kim, Y. V. Kaneti, Y. Yamauchi, *ACS Appl. Mater. Interfaces* **2018**, *1*, 2007–2015.
- [33] B. Liu, H. Shioyama, H. Jiang, X. Zhang, Q. Xu, *Carbon* **2010**, *48*, 456–463.
- [34] C. Vix-Guterl, E. Frackowiak, K. Jurewicz, M. Fribe, J. Parmentier, F. Béguin, *Carbon* **2005**, *43*, 1293–1302.
- [35] H. Jiang, J. Ma, C. Li, *Adv. Mater.* **2012**, *24*, 4197–4202.
- [36] L. Peng, X. Peng, B. Liu, C. Wu, Y. Xie, G. Yu, *Nano Lett.* **2013**, *13*, 2151–2157.

Manuscript received: November 8, 2022

Revised manuscript received: December 11, 2022

Accepted manuscript online: December 13, 2022

Version of record online: January 3, 2023